Nanoscale

PAPER

View Article Online
View Journal

Cite this: DOI: 10.1039/d6nr01170e

Electroreduction of carbon dioxide (CO_2) at oxalate and polypyrrole modified copper surfaces

Minyoung Kim,[a] Meredith Zannacker,[b] Yuxuan Zhang,[a] Reilly Eiynck,[b] Reese Resheske,[b] Donghun Lee,[a] Ella Mack,[b] Elijah Behnke,[b] Sunghwan Lee *[a] and Sujat Sen *[b]

Received 24th March 2026,
Accepted 23rd May 2026

DOI: 10.1039/d6nr01170e

rsc.li/nanoscale

The electrochemical conversion of CO_2 into useful chemicals remains an active area of investigation, especially towards higher order C_2 and C_3 products such as ethylene, ethanol and *n*-propanol. Herein, we demonstrate that oxalate modified copper surfaces on porous gas-diffusion electrodes (GDEs) can be used to modify the selectivity of the electrochemical CO_2 reduction reaction (eCO_2RR) towards higher order chemicals using a flow-type electrochemical cell at near-neutral pH and industrially viable current densities. These multi-layer composite cathodes consisting of a Teflon substrate, coated with copper, and then modified with copper oxalate exhibit up to 79% selectivity to C_{2+} products at varying current densities ranging from 50 up to 250 mA cm^{-2}, representing a shift in electrocatalytic behavior as compared to the pristine copper/Teflon cathode. The oxalate modified copper surface enables further modification with a conductive polymer such as polypyrrole, tunable to varying thicknesses, demonstrating the feasibility of performing oxidative electropolymerization on copper-based GDEs and subsequently using them for the eCO_2RR. We also investigate the changes occurring in these electrodes with respect to particle/grain size, morphology and surface chemistry using SEM, XRD and XPS.

Introduction

The continued development of catalysts and electrode structures for the electrochemical conversion of carbon dioxide (CO_2) to value added chemicals remains of considerable interest worldwide in both academic[1] and industrial settings.[2] Gas phase delivery offers an approach whereby gaseous CO_2 is fed into an electrolysis cell and interfaces with a liquid electrolyte or an ion-selective membrane *via* gas diffusion electrodes (GDEs) that have a catalytic layer.[3] In this configuration, the high diffusive fluxes of gaseous CO_2 enable increased current densities relative to designs using liquid-phase CO_2 delivery. Conventionally, a GDE is prepared by depositing an ink containing catalyst particles onto a gas diffusion layer (GDL). While the use of GDEs enables a dramatic increase in current density, typically an order of magnitude or larger, over atmospheric liquid-phase cell designs, multiple studies have now demonstrated and explained the challenges related to flooding of these structures,[4] which abruptly affects the catalytic performance. Such catastrophic flooding events have been attributed to pressure imbalance across the electrode structure, but primarily due to the deposition/precipitation of carbonate salts from the interaction of gaseous CO_2 and typically alkaline electrolyte (*e.g.* 1 M aqueous KOH). Alternative materials such as polytetrafluoroethylene (PTFE or Teflon) have also been recently investigated for use as porous GDLs on which appropriate catalysts have been deposited through a variety of methods such as sputtering, dip coating, vacuum filtration and other physical/chemical vapor deposition techniques.[5] These porous substrates are typically available commercially in the form of filter discs with variable pore sizes (0.1–0.5 micron) and nominal thicknesses (100–400 micron), sometimes backed by a supporting polymer layer for mechanical reinforcement. The primary benefit of using these Teflon substrates has been the significantly higher resistance to electrolyte flooding as reported by multiple studies and research groups.[6,7] However, the use of such substrates also means coming up with new and modified methods to make electrical contact with the catalyst as Teflon is an electrically insulating material.[6] Furthermore, highly alkaline media (pH 13–15)[6,8] have also been successfully used to suppress the competing hydrogen evolution reaction (HER) that is thermodynamically feasible under the conditions of the electrochemical CO_2 reduction reaction (eCO_2RR). However, more recent studies have cited the need for neutral and even acidic pH media in eCO_2RR systems to improve overall energy efficiency metrics.[9,10]

[a]*School of Engineering Technology, Purdue University, West Lafayette, IN, 47907, USA. E-mail: sunghlee@purdue.edu*
[b]*Department of Chemistry & Biochemistry, University of Wisconsin–La Crosse, La Crosse, WI, 54601, USA. E-mail: ssen@uwlax.edu*

A number of studies have investigated the electrochemical conversion of CO_2 to C_1 products and more recent studies have increasingly focused on the generation of C_{2+} chemicals,[11–15] given their higher intrinsic and often commercial value. Many of these chemicals are commodity chemicals produced through traditional thermochemical methods using fossil fuel-based sources. Due to the higher energy density of *n*-propanol (*n*-PrOH), it could potentially replace conventional fuels[16] or at the very least serve as a superior fuel additive, *e.g.*, replace the ethanol (EtOH) added to gasoline at the pump. Hence, it is attractive to explore whether *n*-PrOH could be generated efficiently through electrolysis using renewable electricity and catalysts that are stable, efficient, abundant, and cheap.

Modification of the copper surface has been investigated through a variety of means. Most notably, the studies by Kanan *et al.*[17] demonstrated that oxide-derived copper exhibits a significant shift in product selectivity compared with the pristine equivalent. Several additional studies have investigated the role of oxide-derived copper synthesized through various thermochemical/electrochemical treatments, resulting in restructured surfaces that promote C–C coupling events leading to higher order hydrocarbons.[18–23] Additional studies have also performed in-depth investigations into the mechanistic aspects of this observed shift in catalytic behavior, attributed to sub-surface oxygen[20] species allowing for a special coordination environment with CO_2 and its intermediates. Evidence of a rich population of undercoordinated sites $Cu^{\delta+}$($0 < \delta < 1$)[24] has been more recently presented in the form of high resolution X-ray photoelectron spectroscopy (XPS) scans and Auger spectra. It has also been suggested that oxide-derived copper promotes higher local pH,[25] promotes chemisorption of CO intermediates,[26] and enhances grain boundaries.[27] Finally, theoretical studies[28] have also been proposed to explain the enhanced activity of copper metal embedded in an oxidized matrix to promote CO_2 activation and CO dimerization to deeply reduced products. However, conclusive proof remains elusive that can explain how these *meta*-stable copper sites can remain active in spite of the thermodynamic considerations of the highly reducing environment under which the eCO_2RR is typically conducted.[29–32]

These studies motivate further investigation into the use of Cu-based catalysts, particularly regarding the impact of surface modification and processing on gas-diffusion type electrodes that are necessary to move from lab to industrial scale implementation of this technology. Towards this goal, physical vapor deposition (PVD) techniques[5,33,34] have also been used to generate layers of catalysts and their performance has often been found to differ as compared to their conventional counterparts. These include sputter coating, e-beam evaporation, and thermal evaporation methods, which are all scalable methods that would allow for rapid production of multi-layer GDE-type composite cathodes with accurate control of layer thickness.

Organic/inorganic hybrid interfaces have also been actively investigated in the past decade for the eCO_2RR.[35] These include a variety of organic moieties with appropriate functional groups that can interact with CO_2 as well as bind to the metal catalyst through physical or chemical methods. Polypyrrole (pPy) and other conductive polymers such as polyaniline have been widely explored as candidates for such organic/inorganic hybrid interfaces across a variety of electrochemical applications given their low cost, intrinsic electrical conductivity, ion exchange mechanisms and ease of synthesis.[36] Specifically discussing the use of pPy for the eCO_2RR, existing studies that have used pPy/copper interfaces have done so using conventional chemical methods for synthesizing the catalyst (*e.g.* solvothermal) followed by casting of the catalyst onto electrodes using physical methods such as drop-casting or spray coating.[37] In contrast, electrochemical polymerization of pyrrole onto a variety of metallic substrates has been demonstrated to produce uniform, highly adherent and highly controllable thin films of varying thicknesses from <50 nm to several microns, which is not the case for conventional chemical polymerization methods.

Select studies have successfully electropolymerized pyrrole onto planar metallic copper surfaces, which in principle poses a challenge given their relative thermodynamic potentials for oxidation, *i.e.* E° for copper oxidation (0.34 V *vs.* SHE) is less than E° for pyrrole (>0.5 V *vs.* SHE) electro-polymerization.[38] In order to prevent the continuous dissolution of the copper surface during the polymerization of pyrrole, prior studies[39–42] have previously reported on the passivation of the copper electrode surface using oxalate salts or oxidative scanning in the presence of oxalic acid electrolytes. The *in situ* created copper oxalate has a very low solubility in aqueous media (pK_{sp} = 10.6)[43] and is mechanically stable, forming a semi-stable surface on which further oxidation of pyrrole can take place. The electrochemical behavior of copper in the presence of complexing agents such as phosphoric or oxalic acids has been investigated for industrial applications, especially in chemical mechanical planarization (CMP)[44] and post-CMP cleaning. However, the use of oxalate-derived copper surfaces as catalysts has not been previously explored for the eCO_2RR. Collectively taken, practical eCO_2RR electrolyzers must be able to operate at acidic or neutral pH[45,46] and at industrially relevant current densities >100 mA cm^{-2}. A brief summary of recent publications that employ gas-phase reactant delivery with a Teflon-based GDL, Cu-based catalysts and near-neutral pH media can be found in Table S1 (SI).

In this study, we investigate the performance of two composite catalysts, namely (a) copper oxalate derived surface and (b) polypyrrole coated copper surface. We find that the oxalate-derived catalyst is more selective for C_{2+} products, especially *n*-PrOH, produced at efficiencies as high as ~12 ± 3% compared to the <3 ± 0.3% efficiency at the pristine copper counterpart under equivalent conditions. Using DFT studies, we attribute this enhanced catalytic behavior to the favorable reaction energetics for recently identified intermediates involved in the production of C_{2+} species. We demonstrate that these copper-oxalate coated GDEs can be further modified with layers of a conductive polymer like polypyrrole (pPy) that is in turn used for the eCO_2RR. The use of the pPy-coated GDE

shows marked suppression of oxygenate product formation in favor of hydrocarbon products such as ethylene. We provide an analysis of the changes occurring in the particle size, morphology and surface chemical composition using a combination of XPS, XRD and SEM. Furthermore, we demonstrate that the thickness of these individual layers of the composite catalyst – either the copper oxalate or polypyrrole – can be controlled carefully from a few 100 nm to several microns accurately through electrochemical means – this would enable careful control over the properties of the catalyst and custom design to a given reactor size. Finally, all tests are performed under neutral pH conditions that are favorable for industrial application, distinct from multiple recent studies that use highly alkaline electrolytes.

Experimental

Electrochemical cell design and setup

GDEs were prepared by thermal evaporation of copper onto commercially available porous Teflon substrates. Additional details are provided in the SI. All electrochemical experiments were performed at room temperature in a custom-built small volume flow cell, which was adapted from a previous report[3] and included separate liquid flow channels, one for the catholyte and another for the anolyte, separated by a membrane. Each catalyst coated GDE (cathode side) was cut with scissors into smaller pieces to be used in the electrolysis experiments. In order to make electrical contact, the rubber gasket next to it was covered at the edges using commercially available copper tape as shown in Fig. S2. The electrolyte channel (cathode side) contains a window of 1.5 cm × 1.7 cm (2.55 cm^2) where the electrolyte interfaces with the catalyst layers, which defines the maximum geometric active area for the cell, and a 1/4 in. circular port approximately in the middle of the 0.5-in. thick channel to accommodate a reference electrode (Ag/AgCl, +210 mV *vs.* SHE), which enables three-electrode operation. The electrolyte channel on the anode side was similar (1.5 cm × 1.7 cm window and 0.25 inch thickness) but did not contain a reference port. All CO_2 reduction electrolysis experiments were conducted using an Ag/AgCl electrode unless stated otherwise. Additional details are available in the SI (S2). Nickel foam (MTI Corporation, 1.6 mm thickness) was cut into appropriate sizes and used as the counter electrode for all electrolysis experiments, unless specified otherwise. A Fumasep (FBM) bipolar membrane (Fuel Cell Store) was used to separate the anode and cathode flow cell chambers, effectively isolating the anolyte and catholyte streams and minimizing product crossover. It was pre-treated as per the manufacturer's recommendations and then soaked in the 1 M $KHCO_3$ electrolyte for at least 24 hours prior to use.

Electrodeposition of copper oxalate and polypyrrole

Copper oxalate thin films were grown directly on the surfaces of pristine Cu-coated TE35 substrates (1000 nm), which were used without any further modifications. Electrodeposition was conducted in the same cell design described above but modified to be a single compartment flow cell without any separator. pPy was electrodeposited on top of the copper oxalate films, and its thickness was controlled by measuring the charge passed. Additional details are available in the SI (S3).

Electrolysis experiments and product quantification

Typically, galvanostatic electrolysis was performed for at least 1 hour or longer. The reported faradaic or current efficiency values were derived from the average current over 1 h and the average product concentrations of 4–5 GC runs, taken at intervals of 12 min, started 5 min after initiating electrolysis. All electrolysis experiments were repeated at least twice, and average values are reported herein. The concentrations of the gas phase products were found to be stable within ±5% during the course of a 1 h electrolysis. Liquid-phase products were quantified using solvent-suppressed 1D ^{1}H NMR (400 MHz, Bruker Avance) at the end of the electrolysis experiment, as per previously reported procedures.[3] Currents reported throughout the manuscript were normalized to the cathode geometric area (2.55 cm^2) to obtain current densities. All experiments were carried out under *iR*-corrected conditions and faradaic efficiency calculations were performed as reported in prior studies.[3] Additional details are provided in the SI (S2).

Ex situ characterization

Micrographs were acquired using instruments at both institutions: either a Zeiss EVO HD scanning electron microscope (SEM) equipped with a Bruker energy-dispersive spectrometer at 20 kV acceleration voltage or alternatively using a Quanta 3D FEG Dual-Beam SEM at an acceleration voltage of 20 kV. Samples were prepared by fixing them onto a stainless-steel stub (Ted Pella Inc.) with carbon adhesive tabs (Ted Pella Inc.), but without the use of a conductive coating. X-ray diffractograms (XRD) were obtained using a Bruker D8 Discovery instrument with Cu Kα radiation (Λ = 0.15406 nm) in Bragg–Brentano geometry working at 50 kV and 1000 μA, using a Vantec 500 area detector. Optical images were taken using an AF202 digital inspection camera (AmScope).

XPS data were acquired using a Thermo Fisher instrument equipped with a monochromatic Al Kα, argon ion sputtering beam source and a gas cluster ion bombardment source. Survey scans were conducted using a 200 eV pass energy and a 400 micron aperture averaged over 2 scans. High resolution scans were taken with a pass energy of 50 eV averaged over 10 scans for each element. The deconvolution and analysis of the high-resolution core-level binding energy spectra were performed using XPSPEAK software (Version 4.1). For the detailed analysis of the Cu $L_3M_{4,5}M_{4,5}$ Auger spectra, CasaXPS software was employed to distinguish and quantify the copper oxidation states. The fitting model for the Auger spectra was constructed based on the characteristic peak parameters and line shapes reported by Biesinger,[47] as well as the experimental peak signatures obtained from the copper oxalate sample synthesized in this study.

Results and discussion

Preparation and analysis of copper-coated GDEs

Fig. 1a shows an optical image of the copper-coated Teflon (TE35) substrate that was used as the GDE in this study. This was prepared using PVD techniques described in section S1. Sheet resistance measurements using the 4-point probe method confirmed a nominal electrical conductivity of approximately 0.018 Ohms per square. The deposition of Cu films (1000 nm thick) visibly appears to be uniform on the surface of the TE35 substrate, and closer inspection using the SEM (Fig. 1b–f) reveals an excellent coverage with distinct nano-sized particles visible at high magnification. These particles were seen to be approximately 100–500 nm in diameter (Fig. 1e), with some particles coalescing together to form larger agglomerates. Lower magnification images also show that the particles follow the contours of the fiber-like structure of the underlying substrate, but the origins of this pattern are not clear when compared to the original substrate (Fig. S1). The microstructure of copper-deposited TE35 (Cu/TE35) was also examined using a SEM image from a cross-sectional view (Fig. 1d), which revealed a distinct vertical texture within the copper layer characteristic of the film growth direction. The thickness was observed to be approximately 1 μm, consistent with the intended synthetic goals.

The successful deposition of a Cu layer on the GDL TE35 substrate *via* thermal evaporation was further corroborated by XRD analysis, as shown in Fig. 1g. The Cu/TE35 sample exhibited characteristic diffraction peaks corresponding to the cubic Cu phase (PDF 04-009-2090), specifically the (111), (200), and (220) peaks located at 2θ values of 43.33°, 50.45°, and 74.15°, respectively. These polycrystalline Cu signals were observed alongside minor peaks arising from the TE35 substrate at 2θ in 20–40°, as confirmed by the bare TE35 pattern (black line). Furthermore, the absence of any discernible peaks corresponding to copper(I) or copper(II) oxide patterns indicates that no significant oxidation of the surface occurred during or after the deposition process. To further evaluate the crystallinity of the deposited copper in the Cu/TE35 sample, the average crystallite size was calculated using the Scherrer equation based on the Cu (111) and (200) peaks (Table S2). The resulting average crystallite sizes were determined to be 18.55 nm and 11.70 nm, respectively, for Cu (111) and (200), which are significantly smaller than the particle dimensions observed in the SEM image in Fig. 1e, indicating that the thermally evaporated particles are polycrystalline in nature and composed of multiple smaller crystallite domains.

Electrodeposition of copper oxalate on the copper-based GDL

In order to prevent the continuous dissolution of the copper surface during the polymerization of pyrrole, copper-coated TE35 substrates were first modified with oxalate layers of varying thicknesses. The slow oxidative scanning is shown in SI Fig. S3, which suggests gradual passivation of the copper electrode surface with copper oxalate. Based on the decreasing currents in the cyclic voltammogram and higher values of internal resistance measured after the deposition process, this copper oxalate layer is less electrically conductive than the original copper surface. This behavior on porous substrates was found to be consistent with prior reports that have explored the electrodeposition of oxalate on planar copper surfaces.[39–41,48] A minimum of 3 cycles of cyclic voltammetry was reported by these studies to be necessary to create a stable oxalate layer on top of which additional layers of polymer were deposited, consistent with our investigation.

To further explore the effect of the number of cycles on morphology, thickness and grain size, copper oxalate samples were prepared at a constant scan rate but with an increasing number of cycles. These are hereon referred to as CuOA 3, CuOA 10, and CuOA 50, where the number indicates the number of cycles scanned during the deposition. Photographs of these passivated surfaces are shown in Fig. 2a–c, revealing a grey-colored surface that becomes progressively more uniform (with fewer patches) and acquires the characteristic blue color of copper oxalate powder. Notably, similar trials of oxalate deposition on commercially available planar copper substrates

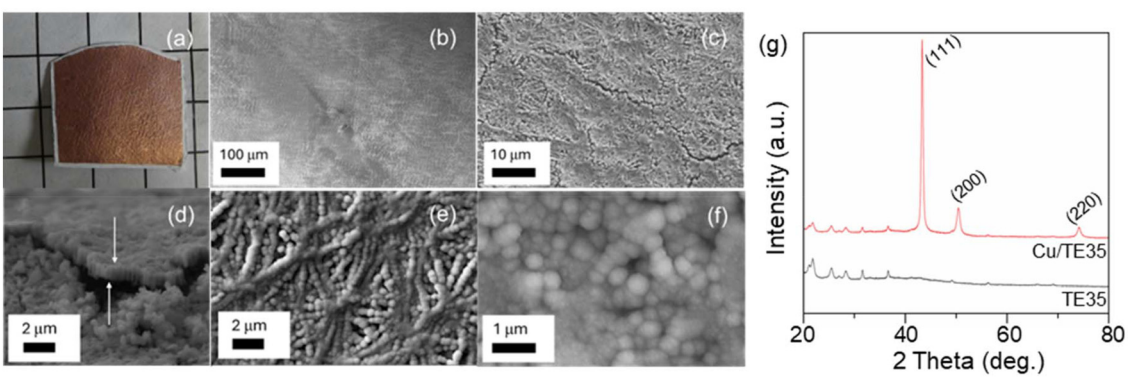

Fig. 1 (a) Photograph of the pristine copper-coated Cu/TE35 substrate with 1 cm grid paper in the background; (b–f) SEM images for the same pristine Cu/TE35 electrode at various magnifications (scale bars included); (d) cross-sectional view obtained from an exposed edge of a cracked region of the film. (g) XRD patterns of the TE35 and Cu/TE35 samples with characteristic Cu peaks indicated (PDF 04-009-2090).

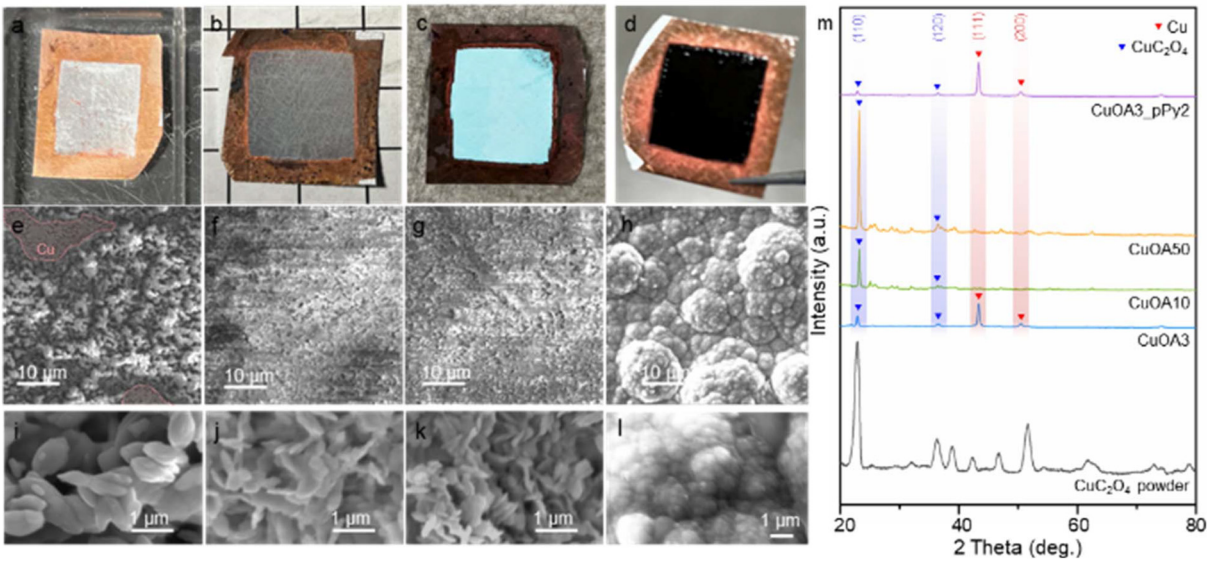

Fig. 2 Analysis of copper-coated TE35 samples modified further by cyclic voltammetry in the presence of oxalic acid for different numbers of cycles: CuOA 3, CuOA 10, CuOA 50 and CuOA3_pPy2. Photographs shown in a–d indicate a modified surface within the 1.5 cm × 1.7 cm rectangular deposition window. Top-view SEM images are shown in e–h and high-magnification SEM images are shown in i–l. Scale bars are included. (m) XRD patterns of the CuOA 3, 10, 50 and CuOA3_pPy2 samples and reference CuC_2O_4 powder with characteristic Cu (PDF 04-009-2090) and CuC_2O_4 (PDF 04-021-4364) peaks indicated.

did not yield uniform thin films, but rather scattered and patchy deposits as seen in Fig. S4. This could be due to a lack of adhesion of the growing oxalate layer onto the planar metal surface, unlike the porous substrate, and this aspect will be explored further in future studies.

The thicknesses and surface morphologies of the copper oxalate-deposited samples were analyzed using SEM images. For the CuOA 3 sample, the cross-sectional image (Fig. S5a) exhibited a distinct bilayer structure. The relatively larger copper oxalate particles covered the copper layer, which retained the characteristic vertical texture as previously observed in the cross-sectional image of Cu/TE35 in Fig. 1d. The thickness of the copper layer in CuOA 3 was ~1.09 µm, and the copper oxalate layer was ~0.988 µm. The top-view SEM image of CuOA 3 (Fig. 2e) showed a surface covered with the oxalate particles; however, some areas indicated that the underlying copper layer might not have been completely covered. In contrast, the CuOA 10 sample displayed a surface completely covered with copper oxalate particles (Fig. 2f), and the characteristic vertical texture of the copper layer observed in Cu/TE35 was not apparent in its cross-sectional image (Fig. S5b). Consequently, a clear interface between the copper and copper oxalate layer was challenging to delineate precisely. The morphology of the cross-section appeared to consist of a relatively smooth top layer, presumed to be copper oxalate, and a bottom layer composed of smaller particles, presumed to be copper; the overall catalyst layer thickness was ~1.44 µm. The CuOA 50 sample also exhibited a surface completely covered with copper oxalate particles (Fig. 2g) with an overall catalyst layer thickness of ~2.90 µm (Fig. S5c). The particle size of the copper oxalate also varied significantly with the extent of electrodeposition, as determined from SEM images (Fig. 2i–k). The CuOA 3 sample exhibited the largest average particle size at 1.50 ± 0.40 µm (Fig. S6a). For the CuOA 10 sample (Fig. S6b), the average particle size significantly decreased to 0.459 ± 0.20 µm. The CuOA 50 sample (Fig. S6c), with the highest electrodeposition charge, showed the smallest average particle size, measured at 0.109 ± 0.35 µm.

XRD analysis was performed to investigate the crystal structure and average crystallite size of the copper oxalate deposited samples (Fig. 2m). The XRD pattern of the CuOA 3 sample exhibited new peaks matching those of copper oxalate powder (CuC_2O_4, PDF 04-021-4364), while also preserving the strong peaks from underlying Cu/TE35, implying that an additional copper oxalate phase layer was successfully electrodeposited onto the Cu/TE35 substrate. Notably, as the number of deposition cycles increased, the diffraction peak corresponding to crystalline Cu diminished completely for the CuOA 10 and CuOA 50 samples, while the peaks from deposited CuC_2O_4 clearly appeared. The diminished Cu signal in XRD indicates that the underlying Cu layer was largely consumed during the copper oxalate conversion process. In addition, since SEM primarily revealed a bulk surface morphology rather than internal microstructures, we further investigated the nanoscale crystallinity by estimating the average crystallite sizes of the Cu and electrodeposited copper oxalate phases using the Scherrer equation from two representative diffraction peaks from each phase: (111) and (200) for Cu and (110) and (120) for the copper oxalate phase (Table S2). CuOA 3 exhibited crystallite sizes of 22.60 nm and 13.54 nm for Cu (111) and (200), respectively, whereas CuOA 10 and 50 did not show any analyzable diffraction peak of Cu. For the CuC_2O_4 phase, CuOA 3 exhibi-

ted the smallest crystallite sizes for both (110) and (120) peaks of 23.82 nm and 10.23 nm, which then gradually increased upon repeating the electrodeposition cycles. The CuC_2O_4 crystallite size of (110) was 33.47 nm and 33.28 nm for 10 and 50 cycles, respectively, and that of (120) was 13.81 nm and 18.28 nm for 10 and 50 cycles. The smallest crystallite size of the copper oxalate phase in CuOA 3 suggests a higher degree of defectiveness and/or structural disorder, which could significantly affect electrocatalytic performance. Specifically, as widely reported in the *e*CO_2RR literature,[27,49] such defect-rich and structurally disordered domains can provide a higher density of catalytically accessible sites and favorably modify intermediate binding behaviors, thereby enhancing the overall catalytic activity.

Electrodeposition of polypyrrole on the copper-based GDL

Using the oxalate modified films, pPy was successfully grown by applying a constant potential. The charge passed during the deposition was used to control the approximate thickness of the pPy layer on top of the copper oxalate sub-layer. The pPy-coated electrodes were prepared by controlling the duration of electropolymerization to control the polymer thickness (they are henceforth referred to as CuOA3_pPy*X*, where *X* indicates the total charge passed during the electropolymerization process) and used further in electrolysis testing. Using cross-sectional images generated *via* FIB-SEM, distinct layers of copper, copper oxalate and the polymer were visible, indicating successful deposition of both oxalate and the polymer (Fig. S7). The thicknesses estimated from these images were found to be consistent with the cross-sectional SEM analysis previously shown in Fig. S5. Furthermore, FTIR analysis confirms the presence of oxalate and polypyrrole specific peaks (Fig. S8). Additional discussion on the characterization using SEM, FTIR and XRD is available in the SI (S4).

Electrochemical reduction of CO_2 at copper and surface-modified electrodes

The as-prepared oxalate coated copper electrodes exhibited significant resistance (25–100 Ohms cm^{-2}) given the oxidized nature of the surface, and as such, they were all subjected to a pre-reduction treatment as described in section S2. Such a practice of pre-reduction or activation before electrolysis testing has been reported in the literature, especially when oxide-derived precursor catalysts are used.[50] After this pre-reduction, the surface was again examined, and Fig. S10 shows the SEM micrographs of the three oxalate modified samples at low and high magnifications. All three oxalate coated samples were found to revert to a similar spherical morphology that was observed initially before oxalate modification (see Fig. 1), albeit with varying particle sizes. Samples also visibly appeared to look like metallic copper without the characteristic blue/grey color of the oxalate layer previously observed. From the low magnification images (Fig. S10a–c), it is clear that pockets or gaps have now been created on the electrode and the underlying porous substrate is visible, particularly for the CuOA 10 and 50 samples. This morphological evolution suggests that significant surface reconstruction occurred even during the mild reduction conditions. Furthermore, high-magnification images (Fig. S10d–f) demonstrate that larger particle clusters were formed in CuOA 10 and CuOA 50 compared to the CuOA 3 sample. This variation in particle size after surface reconstruction can be attributed to differences in the initial particle size, as observed in Fig. 2i–k. Such excessive coalescence inevitably leads to a decrease in the electrochemically active surface area and the annihilation of the thermodynamically unstable yet highly catalytically active surface, which would consequently decrease the overall active sites.[27,51] XRD analysis was also performed for the pre-reduced sample (hereon referred to as an oxalate-derived surface), which confirmed that the oxalate phase was removed and metallic peaks re-emerged, indicating successful electrochemical reduction as shown in Fig. S11.

After this activation or pre-reduction treatment, CO_2 electrolysis experiments were conducted galvanostatically at various current densities using a flow cell for at least 1 h or longer as described in the Experimental section. Equivalent potentiostatic experiments were tried but found to be unstable, leading to *I*/*V* overloads. Fig. 3 and Fig. S12 show the faradaic efficiency (FE) or current efficiency (CE) of the electrolysis process using a pristine copper-coated TE35 GDE made using thermal evaporation (see the Experimental section). It generated a range of gaseous and liquid products detected by gas chromatography (GC) and ^{1}H NMR respectively. Major products (>20% FE) included CO, C_2H_4, H_2 and CH_4, while all liquid products (*e.g.* C_2H_5OH, *n*-PrOH, and HCOOH) were found to account for less than 20% CE. Such trends are consistent with other literature reports that have used metallic copper as a catalyst in a flow cell with gas-diffusion substrates.[46] Cumulatively, the CEs of all C_2 and C_3 products were assessed for all pristine copper (Cu), oxalate-derived CuOA 3 and polypyrrole coated copper (CuOA3_pPy2), as shown in Fig. 3. At pristine copper surfaces, the CEs for such products ranged from 30 to 70% across varying current densities, consistent with prior literature reports that have used similar electrochemical conditions.[46,52,53] Table S1 provides a detailed comparison of the current work using CuOA 3 and CuOA3_pPy2 with comparable reports using copper-based catalysts in a GDE-type flow cell at near neutral pH. For the oxalate modified copper electrode (CuOA 3), the same products were generated at consistently higher CEs across all three current densities ranging from 54 to 79%. Specifically, at 50 mA cm^{-2}, the pristine Cu produced 30% CE as compared to 54% for the oxalate modified electrode, demonstrating a significant shift in selectivity towards higher carbon products. The pPy coated cathode (CuOA3_pPy2) demonstrated efficiencies slightly higher than that of the pristine copper but significantly less than that of the oxalate-derived CuOA 3 surface. Interestingly, a comparison of the hydrocarbon products *vs.* the oxygenates (see Fig. 3) reveals additional trends in catalyst selectivity.[54,55] At low current densities, the selectivity between oxygenates and hydrocarbons is nearly the same across the three samples, although the latter are slightly preferred on the

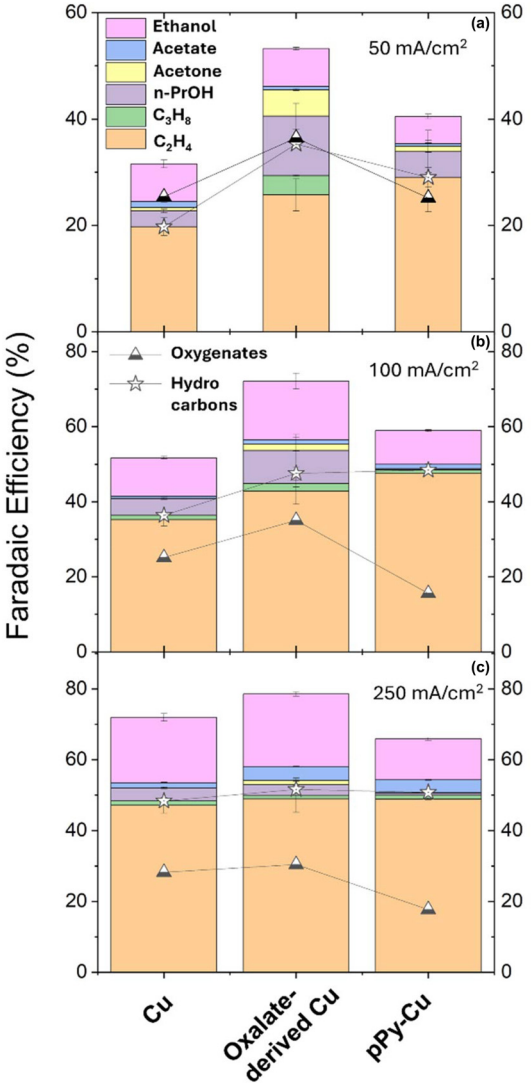

Fig. 3 Plots of faradaic efficiencies specifically to C2 and C3 products generated during electrolysis at pristine copper (Cu), oxalate-derived copper (CuOA 3) and pPy-Cu (CuOA3_pPy2) at various current densities (a: 50 mA cm^{-2}; b: 100 mA cm^{-2}; c: 250 mA cm^{-2}). Cumulative amounts of oxygenates and hydrocarbons are also indicated.

CuOA3_pPy2 sample. This preference for hydrocarbon production over oxygenates becomes much more pronounced at higher current densities for all three samples, but is especially dominant for the CuOA3_pPy2 catalyst. At the same time, this polymer coated catalyst exhibits higher levels of H_2 and CO (see Fig. S12). While such trends align with the literature,[56,57] additional experimental evidence would be needed to corroborate such hypotheses. Notably, these multi-layered composite cathodes exhibited no flooding over the course of 1 h electrolysis at 50 and 100 mA cm^{-2}. For the higher current density electrolysis conducted at 250 mA cm^{-2}, minimal flooding was observed after the cell was taken apart, visible as liquid droplets on the back of the GDL, suggesting that electrowetting phenomena are still relevant as with carbon-based GDLs, albeit more resistant.

Finally, Fig. S13 shows the cathode potential as a function of applied current density during the galvanostatic electrolysis tests. Within the margin of error, the pristine copper and oxalate modified copper cathodes exhibited similar *iR*-corrected potentials across the range of applied currents. However, the CuOA3_pPy2 cathode demonstrated distinctly more negative (higher) cathode potentials, indicating an energy penalty due to the added layer. Such higher potential could also explain the observed increase in H_2 and CO production at CuOA3_pPy2 surfaces (see Fig. S12). These pPy coated samples showed more reproducible results over repeated trials as well as a smaller deviation in cathode potential during the course of 1 h electrolysis (Fig. S14), suggesting possible benefits of the polymer layer for long term operation. However, such claims will need to be further studied *via* long term studies and will be the subject of future studies.

Surface analysis through XPS and post-electrolysis analysis

Given that the chemical state of copper is a critical determinant of the reaction mechanism and product selectivity in the eCO_2RR, XPS was employed to investigate the surface chemical composition and oxidation states of the prepared electrodes. Table S3 summarizes the elemental atomic percentages, calculated by considering the elements of interest (Cu, C, O, N) for each sample. During the electrodeposition process on the copper substrate, as the number of electrodeposition cycles increased from 3 to 50, the surface atomic percentage of Cu decreased from 24.18% in the pristine Cu/TE35 to 10.11% in CuOA 50, accompanied by corresponding increases in C and O content. The gradual attenuation of the Cu signal confirms the successful formation of a copper oxalate overlayer and increased thickness along with deposition cycles, which was also confirmed with the increased thickness observed in the SEM image in Fig. S5. To verify the composition of the deposited layer, the Cu : C : O stoichiometry of the prepared catalyst samples was further analyzed. CuOA 3 showed a distinct increase in the Cu : O ratio (1 : 3.77) compared to the pristine Cu/TE35 (1 : 1.88). With further deposition cycles, CuOA 10 exhibited a Cu : C : O stoichiometry of 1 : 3.05 : 4.01 that most closely matched that of theoretical anhydrous copper oxalate (CuC_2O_4), indicating the successful formation of the target material. However, with additional electrodeposition cycles, the CuOA 50 sample exhibited a higher proportion of oxygen with Cu : C : O as 1 : 4.24 : 4.65. This deviation suggests the potential formation of a hydrated phase ($CuC_2O_4{\cdot}nH_2O$), further supported by the bluish color of the sample's surface (Fig. 2c), which is characteristic of hydrated copper(II) salts. The reduced particle size in CuOA 50 (Fig. S6) further supports the idea, as smaller and more defective morphologies are likely more susceptible to hydration. After the deposition of the pPy layer, CuOA3_pPy2 showed no Cu signal detected, while a significant nitrogen signal (12.30%) emerged, demonstrating the formation of a complete and uniform polypyrrole film covering the underlying substrate. Such a contiguously coated layer implies that the pPy layer could function as a physical and chemical barrier, potentially enhancing the stabi-

lity of the active catalyst during the CO_2 electroreduction reaction.

The modification of the copper surface *via* electrodeposition was further corroborated by high-resolution XPS analysis. In the C 1s spectrum of the CuOA 3 sample (Fig. 4a), a prominent O–C═O peak emerged at 288.40 eV, alongside adventitious hydrocarbons (284.41 eV) and C–O species (286.1 eV).[58,59] This spectral feature distinguishes the oxalate-modified surface from the pristine Cu/TE35 (Fig. S15a), which showed a lower carboxylate signature. The corresponding evidence regarding the oxalate-derived bonding environment was also observed in the O 1s region.[58–60] While the pristine Cu/TE35 (Fig. S15b) exhibited a major Cu–O peak at 531.07 eV (accounting for 92.2% of the total area) from native oxidation under ambient conditions and a minor O–C═C peak at 531.82 eV, the CuOA 3 sample (Fig. S16a) showed a dominance of the oxalate-derived O–C═C peak, comprising 90.68% of the total area, with a minor H_2O signal at 531.73 eV. Notably, in the CuOA 50 sample, the H_2O signal became the dominant feature, occupying 89.79% of the peak area. This significant increase of the H_2O peak confirms that excessive oxalate deposition leads to the formation of a hydrated phase, as previously inferred from its appearance (Fig. 2c) and stoichiometry (Table S3).

The chemical structure of the deposited pPy layer was also elucidated through XPS. In the C 1s spectrum of CuOA3_pPy10 (Fig. 4a), the dominant C–C peak at 284.8 eV and a new peak at 286.6 eV are attributed to the polymer backbone and C═N bonds in the pyrrolic ring, respectively, providing clear evidence of successful polymerization. Furthermore, the peak positions of C–O (286.10 eV) and O–C═O (288.40 eV) observed in CuOA 3 shifted to lower binding energies in the CuOA3_pPy10 sample. This shift implies an increase in the number of carbon atoms bonded to nitrogen, namely C–N (285.80 eV) and $C{=}N^+$ (288.25 eV), which has a lower electronegativity compared to oxygen.[61,62] Detailed information regarding the chemical state of the deposited pPy was obtained from the N 1s spectrum. As shown in Fig. 4b and Fig. S17, neutral pyrrolic nitrogen (NH-Py) at 399.84 eV and positively charged nitrogen species ($C{-}N^+$ and $C{=}N^+$ at 400.92 eV and 402.20 eV, respectively), often referred to as polarons, were both observed in the CuOA3_pPy10 sample. The presence of these species confirms that a conductive pPy overlayer was successfully deposited onto the catalyst layer.

The XPS spectra in the Cu 2p region were analyzed to understand the evolution of copper's oxidation state during the surface modification process (Fig. 4c and Table S4). The deconvoluted Cu $2p_{3/2}$ spectrum of the pristine Cu/TE35 exhibits a peak at 933.55 eV, which accounts for 51.67% of the fitted area and represents a mixture of metallic copper (Cu^0) and copper(I) oxide species since distinguishing Cu^0 from Cu^+

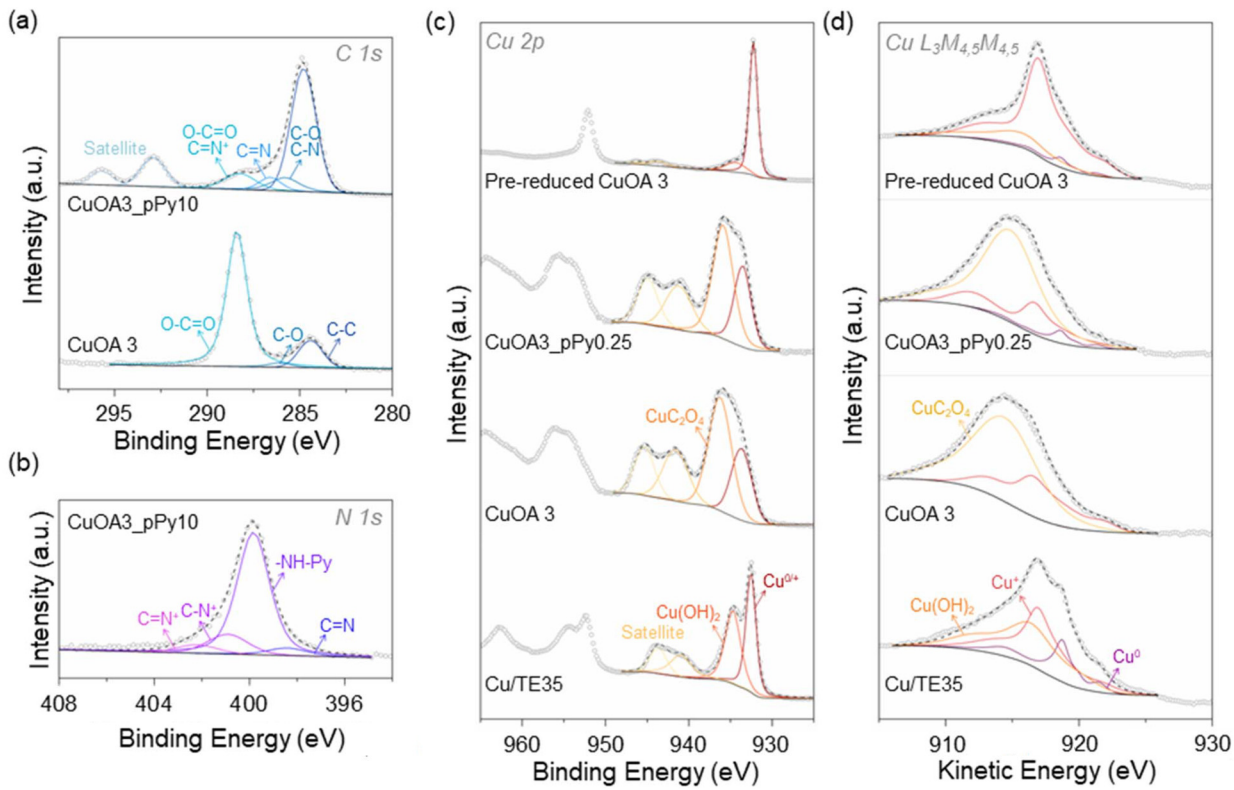

Fig. 4 High-resolution XPS spectra in the (a) C 1s, (b) N 1s, (c) Cu 2p, and (d) Cu $L_3M_{4,5}M_{4,5}$ regions of pristine Cu/TE35, CuOA 3, selected CuOA3_pPy samples, and pre-reduced CuOA 3. CuOA3_pPy10 (thick) was subjected to XPS for the C 1s and N 1s regions, and CuOA3_pPy0.25 (thin) was subjected to XPS for the Cu 2p and Cu $L_3M_{4,5}M_{4,5}$ regions to investigate the surface chemistry of the pPy layer and underlying copper species, respectively.

is challenging based solely on the 2p spectrum due to their overlapping binding energies. Additionally, a Cu^{2+} peak is observed at 934.72 eV (48.33%), likely originating from a thin native oxide layer ($Cu(OH)_2$) formed naturally on the metal surface under ambient conditions. Upon the formation of an oxalate layer in the CuOA 3 sample, a new prominent peak appeared at a higher binding energy of 936.25 eV, which occupies 64.94% of the fitted area. This peak is the characteristic signature of copper oxalate, and it shifted significantly due to the strong electron-withdrawing effect of the coordinating carboxylate ligands.[58,59,63] Notably, the $Cu^{0/+}$ peak shifted positively from 933.55 eV (pristine Cu/TE35) to 933.69 eV, suggesting an enrichment of Cu^+ species at the surface. For the samples with thicker oxalate layers, CuOA 10 and CuOA 50 (Fig. S16b), the copper oxalate peak remained dominant; specifically, the area percentage of the oxalate species increased to 84.72% for the CuOA 50 sample, consistent with the XRD and SEM (Fig. 2) results that indicated a significant growth of the copper oxalate phase. To investigate the chemical state of copper beneath the polymer layer, the thinner CuOA3_pPy0.25 sample was examined for XPS in the Cu 2p region. The Cu 2p spectral profile closely resembles that of the CuOA 3 substrate, with the oxalate peak occupying 63.40% of the area, indicating that the chemical state of the underlying copper oxalate was well-preserved during polymerization. However, the $Cu^{0/+}$ peak shifted back to 933.55 eV from 933.69 eV in CuOA 3. This negative shift suggests a potential increase in the metallic Cu^0 component after the pPy deposition process.

Since quantifying the ratio of Cu^0 and Cu^+ species is challenging from the Cu 2p spectrum alone, the Cu $L_3M_{4,5}M_{4,5}$ Auger spectra were deconvoluted to distinguish these species and perform a quantitative analysis (Fig. 4d and Table S4).[58,59,63] The LMM analysis of the pristine Cu/TE35 surface confirms the presence of Cu^0 (19.03%), Cu^+ (40.54%), and $Cu(OH)_2$ (40.43%) species. The detection of the Cu^0 signal indicates that oxidation is limited to the uppermost few nanometers of the surface, while the underlying bulk material retains its metallic Cu state. In the CuOA 3 sample, the Cu Auger signal is dominated by the copper oxalate species (69.44%) and Cu^+ (30.56%), without any metallic Cu^0 signal observed. The absence of the Cu^0 feature suggests that the CuOA layer is sufficiently thick to prevent the detection of the underlying copper metal, as previously confirmed by the cross-sectional SEM images (Fig. S5). Similarly, the CuOA 10 sample (Fig. S16c) exhibits a composition of CuC_2O_4 (63.51%) and Cu^+ (36.49%), maintaining a ratio comparable to that of CuOA 3. The CuOA3_pPy0.25 sample largely reflects the composition of the CuOA 3 substrate even after the conductive polymer layer deposition, with a dominant oxalate signal (70.85%). However, a distinct metallic Cu^0 signal (~5.01%) was detected, which may be attributed to minor copper dissolution or the presence of exposed copper metal areas that were not fully covered with the initial CuOA layer during the polymerization process.

Finally, the effect of the pre-reduction treatment was examined for the pre-reduced CuOA 3 sample (oxalate-derived surface). The characteristic copper oxalate peak completely disappeared in both the Cu 2p and LMM spectra; instead, a weak $Cu(OH)_2$ peak emerged. The Auger spectrum analysis revealed a surface composition dominated by Cu^+ (76.89%) with a minor metallic Cu^0 signal (5.55%). This specific Cu^+-rich surface environment may be a contributing factor to the high C_{2+} selectivity observed in the electrochemical tests (Fig. 3 and Fig. S12).

To investigate the structural and chemical changes in the catalysts under eCO_2RR operating conditions, SEM, XRD and XPS were performed on the electrodes after the CO_2 reduction reaction. Fig. S18 shows the SEM images for pristine copper, CuOA 3 and CuOA3_pPy2 electrodes after undergoing electrolysis. In the case of both the Cu and CuOA 3 electrodes, some restructuring of the particles is seen in the form of larger clusters compared to both the originally deposited electrode (see Fig. 1 and 2) and the activated or pre-reduced electrode (Fig. S10). The post-electrolysis XRD patterns in Fig. 5a confirm that metallic copper is the primary crystalline phase for all catalyst samples, while copper oxalate peaks have diminished for the CuOA 3 and CuOA3_pPy2 samples. The oxalate phase was reduced and did not persist as a crystalline phase under strong reductive conditions, although localized oxidized Cu species may still remain in amorphous or non-crystalline forms. For the Cu (111) peak of all the samples, a positive shift in the 2θ angle was observed, indicating a contraction of the lattice d-spacing after electrolysis. Moreover, significant crystallite growth occurred in all the catalyst samples, which is likely due to an Ostwald ripening mechanism involving dissolution and redeposition in the electrolyte, resulting in minor XRD peaks of copper carbonate hydroxides.[51,64] After the electrolysis, the average Cu (111) crystallite sizes of the Cu/TE35 and CuOA 3 samples increased from 18.55 nm and 22.60 nm to 27.44 nm and 54.64 nm, respectively, showing 18.0% and 49.78% increases in crystal sizes, respectively. In contrast, the CuOA3_pPy2 sample nearly retained its initial crystallite size (25.51 nm), which is a nominal 6.70% size increase, showing remarkable structural stability presumably due to the additional polymer layer. Considering that the crystallite growth mainly occurs *via* a dissolution–redeposition process, the pPy layer likely suppresses this process by acting as a physical or chemical barrier.[65] Such structural stabilization of the catalysts can help maintain a large active surface area by keeping the crystallite size small. It can also be hypothesized that this mitigates changes in the local reaction microenvironment and promotes metastable copper species, which in turn leads to stable catalytic performance.

To probe the redox states of the copper-based catalysts after the eCO_2RR, the Cu 2p and Cu Auger spectra were analyzed (Fig. 5b and c, Fig. S19, and Table S5). Overall, all post-electrolysis samples showed the complete disappearance of the characteristic CuC_2O_4 peak in both spectral regions. Instead, the surface species redistributed into metallic Cu^0, Cu_2O, and Cu–OH, which may have originated from copper-based carbonate hydroxides during electrolysis as confirmed in XRD analysis (Fig. 5a). The extensive formation of $Cu(OH)_2$ is consistent

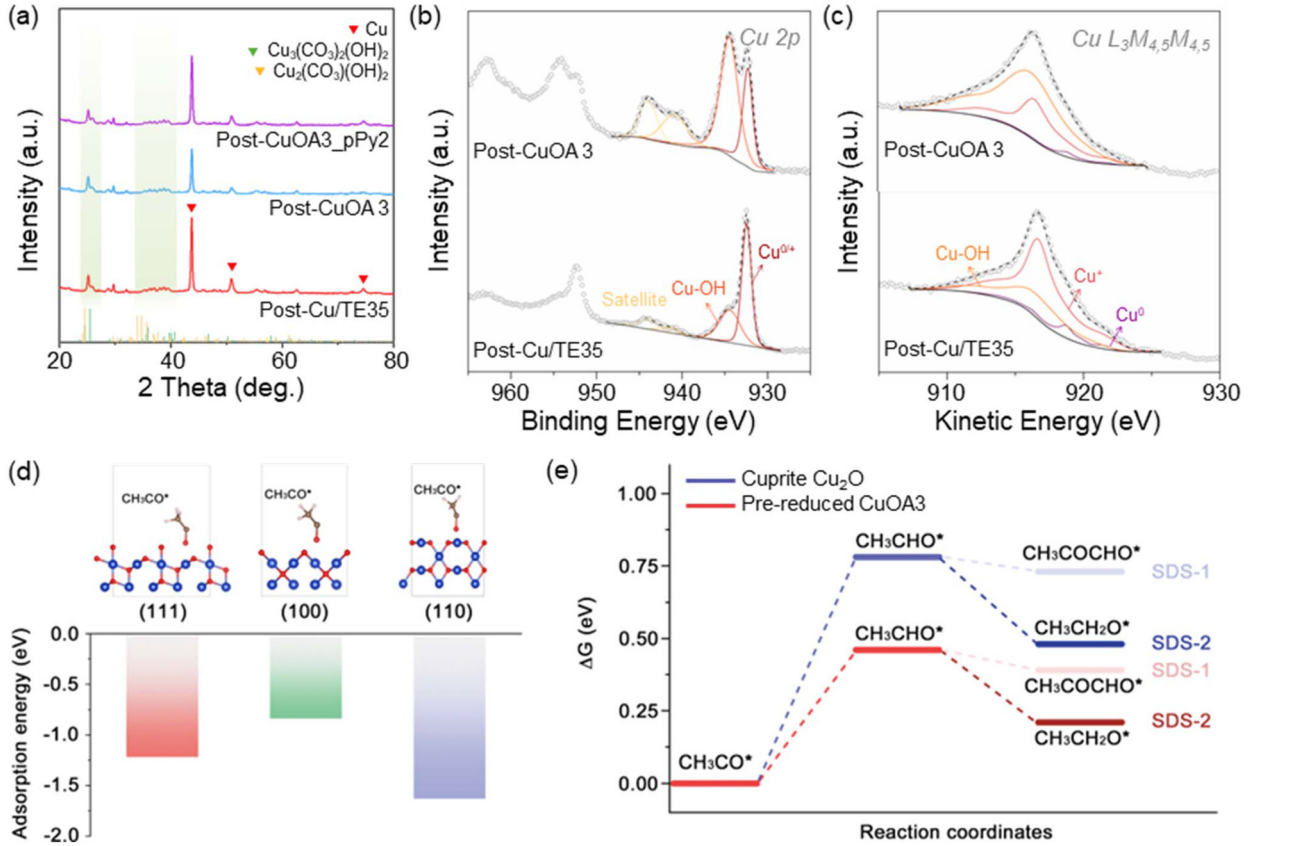

Fig. 5 Post-electrolysis characterization of the catalyst surfaces. (a) XRD patterns of the Cu, CuOA 3, and CuOA3_pPy2 catalysts after CO_2 electroreduction and reference patterns of Cu (PDF 04-009-2090), $Cu_3(CO_3)_2(OH)_2$ (PDF 04-018-0069), and $Cu_2(CO_3)(OH)_2$ (PDF 04-019-0180). (b) High-resolution XPS spectra in the Cu 2p region and (c) Cu $L_3M_{4,5}M_{4,5}$ Auger spectra of the Cu/TE35 and CuOA 3 sample after the eCO_2RR. (d) Calculated adsorption energies of methyl carbonyl on three major facets of the cuprite, along with the corresponding geometric configurations. (e) Calculated reaction energy profiles for the methyl carbonyl-derived reaction pathways on both the cuprite and oxalate-derived surfaces.

with the presence of copper carbonate hydroxides, as previously identified in the post-electrolysis XRD patterns in Fig. 5a. In the Cu 2p region (Fig. 5b), the distribution of oxidation states varied significantly among the samples. For the Cu/TE35 sample, the area percentage of the $Cu^{0/+}$ peak (932.47 eV) increased to 63.70% compared to the pristine state (51.67%), indicating a reduction of the surface during electrolysis. In contrast, the post-CuOA 3 sample exhibited a sharp contrast to its pre-reduced state; the proportion of $Cu(OH)_2$ increased substantially to 67.30%, while the $Cu^{0/+}$ species accounted for only 32.70%. The post-CuOA3_pPy0.25 sample showed a recovery of the $Cu^{0/+}$ fraction to 59.86%, and mild surface etching further increased this proportion to 68.24%. Additional discussion of the changes occurring in the CuOA3_pPy0.25 XPS spectra before and after electrolysis is provided in section S4.

The Cu LMM Auger spectra were further deconvoluted to quantify metallic Cu and Cu^+ species (Fig. 5c). For the post-Cu sample, Cu^+ emerged as the dominant phase (65.25%), while the proportions of Cu^0 (7.26%) and $Cu(OH)_2$ (27.49%) decreased compared to the pre-electrolysis sample. Conversely, the post-CuOA 3 surface was dominated by $Cu(OH)_2$ species (68.01%), with a corresponding Cu^+ content of 29.56% and a minor Cu^0 signal of 2.44%. This composition suggests that the oxalate-derived surface is highly susceptible to reconstruction with a Cu^+-rich surface state, which may contribute to high C_{2+} product selectivity as shown in Fig. 3.[66,67] The impact of the polypyrrole coating is evident in the post-CuOA3_pPy0.25 sample (Fig. S19b and c). The $Cu(OH)_2$ area percentage decreased to 51.58% compared to the uncoated CuOA 3 sample, while the Cu^+ fraction increased to 42.26%. This trend was further pronounced upon etching; the post-CuOA3_pPy0.25-Etch sample revealed an enrichment of reduced species, with Cu^0 increasing to 8.48% and Cu^+ to 49.48%, accompanied by a further reduction in $Cu(OH)_2$ (42.04%). These results corroborate the N 1s analysis, indicating that the conductive polypyrrole sublayer effectively protects the underlying catalyst from excessive dissolution. Considering the higher Cu^+ fraction relative to Cu^0 and the superior C_{2+} selectivity observed for CuOA 3, together with the excellent structural stability of the pPy-modified samples, these findings suggest that simultaneously exploiting these two characteristics could enable the development of eCO_2RR catalysts better suited for C_2^+ production.

Theoretical understanding of the eCO_2RR on oxalate-derived surfaces

As seen in Fig. 3a, the current efficiency for *n*-PrOH production increases to ~12 ± 3% at the oxalate-derived surface compared to the <3 ± 0.3% efficiency at the pristine counterpart under equivalent conditions of 50 mA cm^{-2}. Similarly (per Fig. 3b), the current efficiency for EtOH production increases to ~16 ± 2% at the oxalate-derived surface compared to the ~10 ± 0.3% efficiency at the pristine counterpart under equivalent conditions of 100 mA cm^{-2}. As per the XPS results (Fig. 4) and corresponding Auger analysis (Table S4), we hypothesize that this Cu^{+}-rich surface in this oxalate-derived catalyst (77 *vs.* 40% in the pristine form) is the underlying reason for the observed catalytic behavior and, most notably, the increased production of higher order products such as EtOH and *n*-PrOH. As briefly discussed in the Introduction, there are *in situ* studies that provide experimental evidence that any copper (+1) species are reduced to metallic copper. Simultaneously, there are other operando studies that suggest the presence of metastable or transient copper (+1) species at or near the electrode surface. Hence, conclusive proof of the nature of the constantly restructuring surface under the conditions of eCO2RR remains elusive.[29–32] In order to investigate these enhancements, theoretical calculations were performed with method details provided in section S5.

For both EtOH and *n*-PrOH, the acetyl intermediate (CH_3CHO^*) obtained by the reduction of a methyl carbonyl intermediate (CH_3CO^*) is recognized as a key intermediate and has been reported by recent studies,[68] although this is still an active area of investigation (see Fig. S20). The two selectivity determining steps (SDS-1 and SDS-2) were identified as part of a larger reaction network and were chosen to be the focus of this theoretical study at both the (a) CuOA 3 oxalate-derived catalyst and (b) cuprite surface (Cu_2O). Next, three different Cu_2O facets were chosen, and their adsorption energies with the key intermediate were calculated and compared, allowing us to identify the preferential surface on which the reaction is most likely to initiate. As shown in Fig. 5d, the lowest adsorption energy is seen on the (110) facet, making it most likely to be the anchor site during the early stages of the reaction, where subsequent catalytic transformations are expected to occur.[69,70] The optimized adsorption configurations of related reaction intermediates on both cuprite Cu_2O and oxalate-derived surfaces were also explored (Fig. S21) and subsequently used for the reaction energy barrier analysis.

Next, the reaction energy barriers along the eCO_2RR pathway, identified as SDS-1 and SDS-2,[68] were evaluated on the (110) facet applied to both catalytic systems. Fig. 5e shows that the oxalate-derived surface exhibits consistently lower reaction barriers compared with pristine cuprite along both reaction pathways. For the conversion from the methyl carbonyl intermediate to the acetyl intermediate on the pristine cuprite surface, the reaction energy barrier is calculated to be 0.78 eV, which is higher than that on the oxalate-derived surface (0.46 eV). The subsequent transformations toward either the EtOH precursor or the C_3 intermediate leading to *n*-PrOH are thus energetically more favorable on the oxalate-derived surface, indicating improved reaction kinetics. This behavior can be attributed to the different coordination environments of Cu at the oxalate-derived surface compared to cuprite.

Conclusions

We have demonstrated that copper oxalate can be electrochemically grown on the surface of copper-coated Teflon substrates to various thicknesses using cyclic voltammetry. The resulting oxalate films have varying thicknesses and associated particle shapes and sizes that can be controlled using the total charge passed. This oxalate layer is used as a platform to oxidatively deposit pPy thin films, which are then used as cathodes for the electrochemical conversion of CO_2 in a neutral pH environment and gas-fed flow cells. We demonstrate that the resulting multi-layered composite cathode consisting of Teflon/copper/copper oxalate/polymer layers generates nearly 79% selectivity to C_{2+} products at varying current densities ranging from 50 up to 250 mA cm^{-2}, representing a shift in electrocatalytic behaviour as compared to the pristine copper/Teflon cathode. Specific products such as EtOH and *n*-propanol are observed to have enhanced efficiencies on oxalate-derived surfaces as compared to their pristine counterparts. SEM, XRD and XPS data before and after electrolysis confirm that the oxalate species is reduced to a copper phase, but varying amounts of copper species are found, which offer some insight into the differences in their catalytic performance. Supporting theoretical studies *via* DFT are also presented and suggest lower reaction energy barriers on the oxalate derived surfaces as compared to the pristine, specifically for known reaction intermediates to C_2 and C_3 products of interest. This methodology can be used to carefully control the thickness of pPy films from a few nanometers to several microns with greater accuracy/control unlike widely reported solvothermal methods. It can also be extended to other conductive polymers such as polyaniline, PEDOT or their derivatives, which have been electropolymerized on relatively inert substrates such as steel. Furthermore, this strategy could also be extended to other copper salts that form a water insoluble yet mechanically stable film on copper surfaces such as phosphates, tartrates, and benzoates and explore the changes to their particular morphology upon exposure to eCO_2RR conditions. Finally, additional studies are required to explore the stability related benefits of the polymer coating of this composite cathode structure and how it translates to electrolytes with varying pH values.

Author contributions

Minyoung Kim: investigation, visualization, and writing – original draft. Meredith Zannacker: investigation. Yuxuan Zhang: investigation, visualization, and writing – review & editing. Reilly Eiynck: investigation and writing – original draft. Reese

Resheske: investigation and writing – original draft. Donghun Lee: investigation. Ella Mack: investigation. Elijah Behnke: investigation. Sunghwan Lee: conceptualization, visualization, funding acquisition, project administration, supervision, and writing – review & editing. Sujat Sen: writing – original draft, conceptualization, investigation, visualization, funding acquisition, project administration, supervision, and writing – review & editing.

Conflicts of interest

There are no conflicts to declare.

Data availability

The data supporting this article have been included as part of the supplementary information (SI). Supplementary information: Fig. S1–S21 and Tables S1–S5, including optical photographs, electrochemical measurements, XPS characterization, benchmarking reports for Cu-based CO_2 reduction catalysts, and further experimental details. See DOI: https://doi.org/10.1039/d6nr01170e.

Additional data will be available on request.

Acknowledgements

This work was partially supported by financial support from the U.S. National Science Foundation (NSF) Award No. CBET-2207302 and CBET-2207303. The authors also gratefully acknowledge the use of facilities and instrumentation at the UW–Madison Wisconsin Centers for Nanoscale Technology. The Center (wcnt.wisc.edu) is partially supported by the Wisconsin Materials Research Science and Engineering Center (NSF DMR-2309000) and the University of Wisconsin-Madison. MZ, RE, RR and EM are also grateful to the UWL Undergraduate Research and Creativity Grants for financial support.

References

1 R.-Z. Xiong, H.-M. Xu, H.-R. Zhu, Z.-J. Zhang and G.-R. Li, *Chem. Eng. J.*, 2025, **505**, 159210.
2 X. Zhong, H.-J. Peng, C. Xia and X. Liu, *J. Mater. Chem. A*, 2024, **12**, 19663–19684.
3 S. Sen, S. M. Brown, M. Leonard and F. R. Brushett, *J. Appl. Electrochem.*, 2019, **49**, 917–928.
4 L. M. Baumgartner, A. Goryachev, C. I. Koopman, D. Franzen, B. Ellendorff, T. Turek and D. A. Vermaas, *Energy Adv.*, 2023, **2**, 1893–1904.
5 L. R. Manpatilan, S. Bianco, G. Cicero, J. Zeng and E. Tresso, *ChemSusChem*, 2025, e202500813.
6 C.-T. Dinh, T. Burdyny, M. G. Kibria, A. Seifitokaldani, C. M. Gabardo, F. P. García de Arquer, A. Kiani, J. P. Edwards, P. De Luna, O. S. Bushuyev, C. Zou, R. Quintero-Bermudez, Y. Pang, D. Sinton and E. H. Sargent, *Science*, 2018, **360**, 783–787.
7 M. Filippi, T. Möller, R. Pastusiak, E. Magori, B. Paul and P. Strasser, *ACS Energy Lett.*, 2024, **9**, 1361–1368.
8 Y. Wang, Z. Wang, C.-T. Dinh, J. Li, A. Ozden, M. Golam Kibria, A. Seifitokaldani, C.-S. Tan, C. M. Gabardo, M. Luo, H. Zhou, F. Li, Y. Lum, C. McCallum, Y. Xu, M. Liu, A. Proppe, A. Johnston, P. Todorovic, T.-T. Zhuang, D. Sinton, S. O. Kelley and E. H. Sargent, *Nat. Catal.*, 2020, **3**, 98–106.
9 A. Ozden, F. P. García de Arquer, J. E. Huang, J. Wicks, J. Sisler, R. K. Miao, C. P. O'Brien, G. Lee, X. Wang, A. H. Ip, E. H. Sargent and D. Sinton, *Nat. Sustain.*, 2022, **5**, 563–573.
10 J. A. Rabinowitz and M. W. Kanan, *Nat. Commun.*, 2020, **11**, 5231.
11 C. Long, X. Liu, K. Wan, Y. Jiang, P. An, C. Yang, G. Wu, W. Wang, J. Guo, L. Li, K. Pang, Q. Li, C. Cui, S. Liu, T. Tan and Z. Tang, *Sci. Adv.*, 2023, **9**, eadi6119.
12 Q. Li, J. Wu, C. Yang, S. Li, C. Long, Z. Zhuang, Q. Li, Z. Guo, X. Huang, Z. Tang, H. Li, D. Wang and Y. Li, *J. Am. Chem. Soc.*, 2025, **147**, 6688–6697.
13 S. Jeong, C. Huang, Z. Levell, R. X. Skalla, W. Hong, N. J. Escorcia, Y. Losovyj, B. Zhu, A. N. Butrum-Griffith, Y. Liu, C. W. Li, D. Reifsnyder Hickey, Y. Liu and X. Ye, *J. Am. Chem. Soc.*, 2024, **146**, 4508–4520.
14 G. Wu, Y. Song, Q. Zheng, C. Long, T. Fan, Z. Yang, X. Huang, Q. Li, Y. Sun, L. Zuo, S. Lei and Z. Tang, *Adv. Energy Mater.*, 2022, **12**, 2202054.
15 J. Li, F. Che, Y. Pang, C. Zou, J. Y. Howe, T. Burdyny, J. P. Edwards, Y. Wang, F. Li, Z. Wang, P. De Luna, C.-T. Dinh, T.-T. Zhuang, M. I. Saidaminov, S. Cheng, T. Wu, Y. Z. Finfrock, L. Ma, S.-H. Hsieh, Y.-S. Liu, G. A. Botton, W.-F. Pong, X. Du, J. Guo, T.-K. Sham, E. H. Sargent and D. Sinton, *Nat. Commun.*, 2018, **9**, 4614.
16 Y. Qian, J. Guo, Y. Zhang, W. Tao and X. Lu, *Appl. Therm. Eng.*, 2018, **144**, 126–136.
17 C. W. Li and M. W. Kanan, *J. Am. Chem. Soc.*, 2012, **134**, 7231–7234.
18 R. Kas, R. Kortlever, A. Milbrat, M. T. M. Koper, G. Mul and J. Baltrusaitis, *Phys. Chem. Chem. Phys.*, 2014, **16**, 12194–12201.
19 A. Dutta, M. Rahaman, N. C. Luedi, M. Mohos and P. Broekmann, *ACS Catal.*, 2016, **6**, 3804–3814.
20 A. Eilert, F. Cavalca, F. S. Roberts, J. Osterwalder, C. Liu, M. Favaro, E. J. Crumlin, H. Ogasawara, D. Friebel, L. G. M. Pettersson and A. Nilsson, *J. Phys. Chem. Lett.*, 2017, **8**, 285–290.
21 L. Mandal, K. R. Yang, M. R. Motapothula, D. Ren, P. Lobaccaro, A. Patra, M. Sherburne, V. S. Batista, B. S. Yeo, J. W. Ager, J. Martin and T. Venkatesan, *ACS Appl. Mater. Interfaces*, 2018, **10**, 8574–8584.
22 Z. Lian, F. Dattila and N. López, *Nat. Catal.*, 2024, **7**, 401–411.
23 C. A. Obasanjo, G. T. S. T. Da Silva, F. G. Marin, L. H. Mascaro and C.-T. Dinh, *ACS Catal.*, 2025, **15**, 5706–5717.
24 C. Long, X. Liu, K. Wan, Y. Jiang, P. An, C. Yang, G. Wu, W. Wang, J. Guo, L. Li, K. Pang, Q. Li, C. Cui, S. Liu, T. Tan and Z. Tang, *Sci. Adv.*, 2023, **9**, eadi6119.

25 Y. Pang, T. Burdyny, C.-T. Dinh, M. G. Kibria, J. Z. Fan, M. Liu, E. H. Sargent and D. Sinton, *Green Chem.*, 2017, **19**, 4023–4030.
26 S. Lee, D. Kim and J. Lee, *Angew. Chem., Int. Ed.*, 2015, **54**, 14701–14705.
27 X. Feng, K. Jiang, S. Fan and M. W. Kanan, *ACS Cent. Sci.*, 2016, **2**, 169–174.
28 H. Xiao, W. A. Goddard, T. Cheng and Y. Liu, *Proc. Natl. Acad. Sci. U. S. A.*, 2017, **114**, 6685–6688.
29 B. Ligt, E. J. M. Hensen and M. Costa Figueiredo, *Curr. Opin. Electrochem.*, 2023, **41**, 101351.
30 L. Xu, J. Feng, L. Wu, X. Song, X. Tan, L. Zhang, X. Ma, S. Jia, J. Du, A. Chen, X. Sun and B. Han, *Green Chem.*, 2023, **25**, 1326–1331.
31 X. Zhou, J. Shan, L. Chen, B. Y. Xia, T. Ling, J. Duan, Y. Jiao, Y. Zheng and S.-Z. Qiao, *J. Am. Chem. Soc.*, 2022, **144**, 2079–2084.
32 J.-J. Velasco-Vélez, T. Jones, D. Gao, E. Carbonio, R. Arrigo, C.-J. Hsu, Y.-C. Huang, C.-L. Dong, J.-M. Chen, J.-F. Lee, P. Strasser, B. Roldan Cuenya, R. Schlögl, A. Knop-Gericke and C.-H. Chuang, *ACS Sustainable Chem. Eng.*, 2019, **7**, 1485–1492.
33 E. Jeng, Z. Qi, A. R. Kashi, S. Hunegnaw, Z. Huo, J. S. Miller, L. B. Bayu Aji, B. H. Ko, H. Shin, S. Ma, K. P. Kuhl, F. Jiao and J. Biener, *ACS Appl. Mater. Interfaces*, 2022, **14**, 7731–7740.
34 S. A. Mahyoub, A. Farid, M. Z. Azeem, D. A. A. Fadhil, F. A. Qaraah and Q. A. Drmosh, *Small Struct.*, 2025, **6**, 2400501.
35 L.-Q. Qiu, H.-R. Li and L.-N. He, *Acc. Chem. Res.*, 2023, **56**, 2225–2240.
36 Y. Yesudas K, G. Buvaneswari and A. Senthil Kumar, *Electrochem. Sci. Adv.*, 2025, **5**, e2400007.
37 A. P. Periasamy, R. Ravindranath, S. M. S. Kumar, W.-P. Wu, T.-R. Jian and H.-T. Chang, *Nanoscale*, 2018, **10**, 11869–11880.
38 M. Takakubo, *Synth. Met.*, 1987, **18**, 53–58.
39 C. Gabrielli, L. Beitone, C. Mace, E. Ostermann and H. Perrot, *Microelectron. Eng.*, 2008, **85**, 1677–1685.
40 S. Aksu, *J. Electrochem. Soc.*, 2005, **152**, G938.
41 P. Herrasti, A. I. del Rio and J. Recio, *Electrochim. Acta*, 2007, **52**, 6496–6501.
42 M. Menkuer and H. Ozkazanc, *Prog. Org. Coat.*, 2019, **130**, 149–157.
43 A. V. Levanov, O. Y. Isaikina and V. V. Lunin, *Chem. Eng. Commun.*, 2021, **208**, 1385–1394.
44 Y. Xu, Y. Mao, M. H. Ijaz, M. E. Ibrahim, S. Le, F. Wang, J. Jiang, D. Chi, M. An, S. Song, Y. Huang and Y. Zhang, *J. Electrochem. Soc.*, 2024, **171**, 093506.
45 T. Burdyny and W. A. Smith, *Energy Environ. Sci.*, 2019, **12**, 1442–1453.
46 X. Wang, K. Klingan, M. Klingenhof, T. Möller, J. Ferreira de Araújo, I. Martens, A. Bagger, S. Jiang, J. Rossmeisl, H. Dau and P. Strasser, *Nat. Commun.*, 2021, **12**, 794.
47 M. C. Biesinger, *Surf. Interface Anal.*, 2017, **49**, 1325–1334.
48 O. Devos, C. Gabrielli, L. Beitone, C. Mace, E. Ostermann and H. Perrot, *J. Electroanal. Chem.*, 2007, **606**, 85–94.
49 A. Verdaguer-Casadevall, C. W. Li, T. P. Johansson, S. B. Scott, J. T. McKeown, M. Kumar, I. E. L. Stephens, M. W. Kanan and I. Chorkendorff, *J. Am. Chem. Soc.*, 2015, **137**, 9808–9811.
50 L. Ma, Q. Geng, L. Fan, J.-X. Li, D. Du, J. Bai and C. Li, *Nano Res.*, 2023, **16**, 9065–9072.
51 S. H. Lee, J. E. Avilés Acosta, D. Lee, D. M. Larson, H. Li, J. Chen, J. Lee, E. Erdem, D. U. Lee, S. J. Blair, A. Gallo, H. Zheng, A. C. Nielander, C. J. Tassone, T. F. Jaramillo and W. S. Drisdell, *J. Am. Chem. Soc.*, 2025, **147**, 6536–6548.
52 X. He, L. Lin, X. Li, M. Zhu, Q. Zhang, S. Xie, B. Mei, F. Sun, Z. Jiang, J. Cheng and Y. Wang, *Nat. Commun.*, 2024, **15**, 9923.
53 H. S. Jeon, J. Timoshenko, C. Rettenmaier, A. Herzog, A. Yoon, S. W. Chee, S. Oener, U. Hejral, F. T. Haase and B. Roldan Cuenya, *J. Am. Chem. Soc.*, 2021, **143**, 7578–7587.
54 C. Y. J. Lim, M. Yilmaz, J. M. Arce-Ramos, A. D. Handoko, W. J. Teh, Y. Zheng, Z. H. J. Khoo, M. Lin, M. Isaacs, T. L. D. Tam, Y. Bai, C. K. Ng, B. S. Yeo, G. Sankar, I. P. Parkin, K. Hippalgaonkar, M. B. Sullivan, J. Zhang and Y.-F. Lim, *Nat. Commun.*, 2023, **14**, 335.
55 C. Zhan, F. Dattila, C. Rettenmaier, A. Herzog, M. Herran, T. Wagner, F. Scholten, A. Bergmann, N. López and B. Roldan Cuenya, *Nat. Energy*, 2024, **9**, 1485–1496.
56 H.-J. Peng, M. T. Tang, J. Halldin Stenlid, X. Liu and F. Abild-Pedersen, *Nat. Commun.*, 2022, **13**, 1399.
57 M. Wang, L. Kong, X. Lu and C.-M. Lawrence Wu, *Appl. Surf. Sci.*, 2023, **618**, 156678.
58 S. Chenakin and N. Kruse, *Appl. Surf. Sci.*, 2020, **515**, 146041.
59 S. P. Chenakin and N. Kruse, *Appl. Surf. Sci.*, 2026, **716**, 164671.
60 J. S. Yeoh, I. Di Bernardo, N. G. White, V. Otieno-Alego, T. Tsuzuki and A. Lowe, *Mater. Adv.*, 2021, **2**, 292–302.
61 S. Kim, J.-O. Jeong, S. Lee, J.-S. Park, H.-J. Gwon, S. I. Jeong, J. G. Hardy, Y.-M. Lim and J. Y. Lee, *Sci. Rep.*, 2018, **8**, 3721.
62 J. Tabačiarová, M. Mičušík, P. Fedorko and M. Omastová, *Polym. Degrad. Stab.*, 2015, **120**, 392–401.
63 S. P. Chenakin and N. Kruse, *Appl. Surf. Sci.*, 2024, **669**, 160460.
64 Z.-Z. Wu, P.-P. Yang and M.-R. Gao, *Nano Mater. Sci.*, 2026, **8**, 687–702.
65 M. K. Zadeh, M. Yeganeh, M. T. Shoushtari and A. Esmaeilkhanian, *Synth. Met.*, 2021, **274**, 116723.
66 F. Zhang, N. Cao, C. Wang, S. Wang, Y. He, Y. Shi, M. Yan, Y. Bao, Z. Li and P. Xie, *Nat. Commun.*, 2025, **16**, 6082.
67 R. M. Arán-Ais, F. Scholten, S. Kunze, R. Rizo and B. Roldan Cuenya, *Nat. Energy*, 2020, **5**, 317–325.
68 Y. Xue, X. Lv, C. Yang, L. Song, L. Zhang and G. Zheng, *Chem. Sci.*, 2025, **16**, 13944–13950.
69 Y. Zhang, M. Kim, D. H. Lee, F. Qin, H.-W. Song, C. S. Kim, J. Park, C. Kim, F. Lian and S. Lee, *Energy Environ. Sci.*, 2025, **18**, 3852–3868.
70 Y. Zhang, D. H. Lee, H. Park, S.-J. Chang, J. Baek, B.-H. Jun, J. Park, D. Kim, H. W. Song, D.-K. Ko, H. Park, C. S. Kim and S. Lee, *ACS Appl. Mater. Interfaces*, 2025, **17**, 40810–40825.